Supplementary material: Mottness collapse without metallisation in the domain walls of triangular-lattice Mott insulator 1T-TaS_2

I. HOPPING AMPLITUDES INSIDE THE DOMAIN WALLS OF VARIOUS TYPES

Here we discuss the magnitude of the relative hopping factor r arising from the change in the separation between the Wannier orbitals of David Stars forming the domain wall. As discussed in Ref. 1, the hopping amplitudes in tight-binding Hamiltonians describing transition metals scale as d^{-5}, where d is the distance between the atoms. This fact, combined with the results of Rossnagel *et al.*, Ref. 2, on the reconstructed phase in 1T-TaS_2 showing that the main contribution to the narrow band in the C-CDW phase comes from the orbitals centered in the middle of David stars, allows us to estimate the relative change in the hopping amplitudes inside a DW. As an example, we consider here the three typical DW structures which we enumerate 1,2,4 following Ref. 3; the corresponding schematic plots are shown in Fig. 1. The resulting relative distances and hopping ratios are collected in Tab. I. In a dimerized tight-binding chain with hoppings r_1 and r_2 the band gap is given by $2|r_1 - r_2|$, the width of the interval supporting both subbands by $2(r_1 + r_2)$, the bandwidth of each subband by $2\min\{r_1, r_2\}$, while the occupied band kinetic energy is proportional to $\sqrt{r_1^2 + r_2^2}$. It is this latter scale which controls the boundary Mott metal-insulator transition; for details see Section V. Note that in all three cases considered one of the r values is large; it is this dominant r which leads to an increased kinetic energy and Mottness collapse, with the other r value as a subleading correction. The difference between r_1 and r_2 then additionally leads to the bonding-antibonding splitting of the quasiparticle band as a secondary effect.

DW type	d_1	d_2	r_1	r_2
1	0.83	1.11	2.51	0.6
2	1.21	0.73	0.38	4.7
4	0.73	0.83	4.7	2.51

Table I. Relative distances d_1, d_2 and relative hoppings r_1, r_2 for commonly occurring types of single standing DWs.

II. DOPING-DRIVEN TRANSITION

As described in the main text, the metallisation in the domain wall can also be triggered by modifying the on-site potential on the DW sites, see Fig. 2. With increasing δ, the LHB and UHB shift with respect to the bulk Hubbard bands and the spectral density is redistributed within the bands, although the bandwidths are only weakly affected. As the LHB crosses the Fermi level with increasing δ, the system metallizes at $\delta = \delta_c \approx 1.0D$, see Fig. 2(a), and a QP band emerges at the top of the LHB, see Fig. 2(b). The transition has no hysteresis in this case. As δ increases past δ_c the electron density at the DW rapidly decreases, see Fig. 2(c), i.e., the DW becomes charged. A charged DW in an infinite insulating bulk must be of finite length in order for the electric potential to remain finite and it must be furthermore in contact with a charge reservoir for the charge to flow into the DW during the metallisation: indeed the observed DWs are kinked and often terminate at large lattice inhomogeneities.

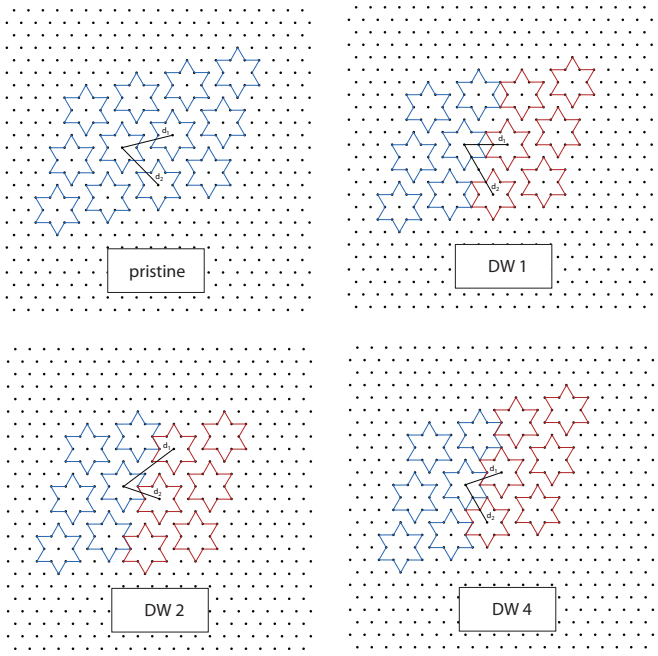

Figure 1. Schematic plot of the superlattice pattern in pristine 1T-TaS_2 and for three commonly occurring domain wall types (1,2,4).

The modification of local potential leads to the experimentally observed gradual shift of the bands towards the Fermi level, see Fig. 1(d) in the main text. The band shift occurs on several sites adjacent to the DW core. On these peripheral sites the spectral shape is maintained but the band approaches the Fermi level. Such behavior results from the long-range part of the Coulomb interaction. From the symmetry of the shift we infer that the source of the potential is the DW core itself.

III. FINE DETAILS IN THE QUASIPARTICLE BAND IN THE BANDWIDTH-DRIVEN MOTT TRANSITION

The Mottness collapse due to increased hopping generates itinerant quasiparticles. These tunnel in the surrounding insulating lattice [4] with a hopping matrix element proportional to $\cos(k/2)$, producing a weakly dispersive spectral feature

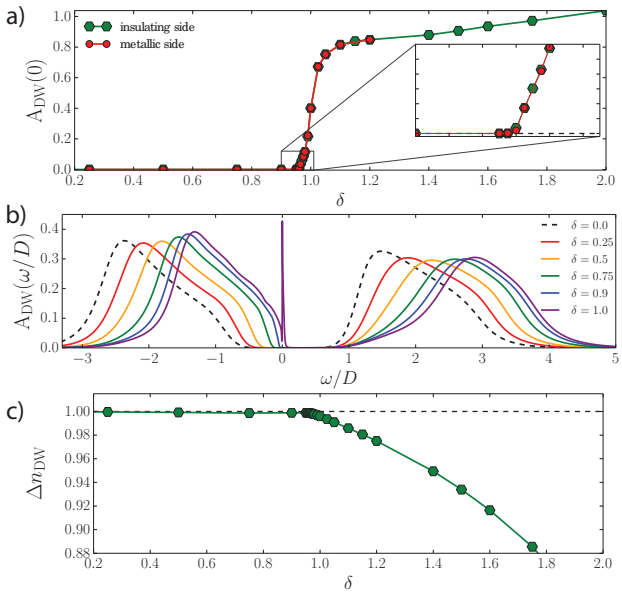

Figure 2. Effects of the on-site potential $\epsilon_{\rm DW} = \epsilon + \delta$, $r = 1$. (a) Local DOS at the Fermi level across the doping-driven Mott transition. (b) Local DOS for select values of δ. (c) Local electron density $n_{\rm DW}$ vs. δ.

at $k \sim 0$ with energy close to that of the pole in the bulk self-energy function (the pole which produces the Mott insulating behavior). The resulting peak S, despite having rather small spectral weight, produces the sequence of two kinks at $r \sim 2.45$ and $r \sim 2.5$ in the Fermi-level LDOS seen in Fig. 4(a) of main text.

IV. DETAILS OF THE R-DMFT CALULATIONS

We employ the real-space DMFT (R-DMFT) to solve the model defined by Eq. (1) in the main text. Within this approach the assumption of spatial homogeneity is lifted and the lattice Green's function, instead of using the Hilbert transform, is calculated using its real-space representation as

$$\hat{\mathcal{G}}_{\rm latt}(z) = \left[z - \hat{\mathcal{H}}_{\rm kin} - \hat{\Sigma}(z)\right]^{-1}, \qquad (1)$$

where $\hat{\mathcal{H}}_{\rm kin}$ is the hopping matrix in the Wannier basis. The hats above $\hat{\Sigma}(z)$, $\hat{\mathcal{G}}_{\rm latt}(z)$, $\hat{\mathcal{H}}_{\rm kin}$ underline the fact that these are matrix quantities. From $\hat{\mathcal{G}}_{\rm latt}(z)$ the site dependent hybridization function $\Delta_i(z)$ is calculated through

$$\Delta_i(z) = z - \left[\hat{\Sigma}(z)\right]_{i,i} - \frac{1}{[\hat{\mathcal{G}}_{\rm latt}(z)]_{i,i}}. \qquad (2)$$

To take advantage of the symmetries in the system we introduce a mixed basis representation by performing a partial Fourier transformation along the domain-wall direction [5, 6]. As a result, the kinetic term in the Hamiltonian is given by

$$\begin{aligned}\mathcal{H}_{\rm kin} = -\sum_{x,k,\sigma} \Big(&2t\cos(ka)\, c^\dagger_{\{x,k\},\sigma} c_{\{x,k\},\sigma} + \\ &+(t_{1,x}e^{-ik\frac{a}{2}} + t_{2,x}e^{ik\frac{a}{2}})c^\dagger_{\{x+1,k\},\sigma} c_{\{x,k\},\sigma} + \\ &+(t^*_{1,x-1}e^{ik\frac{a}{2}} + t^*_{2,x-1}e^{-ik\frac{a}{2}})c^\dagger_{\{x-1,k\},\sigma} c_{\{x,k\},\sigma}\Big),\end{aligned} \qquad (3)$$

where k is the quasi-momentum in the DW direction, x is the distance in perpendicular direction, and a denotes the inter-site distance. Any contributions coming from the non-orthogonality of the triangular lattice basis come as a phase factor and thus can be removed by a unitary transformation of the fermionic operators. In the mixed basis $\mathcal{H}_{\rm kin}$ becomes block diagonal with each block describing a one-dimensional system in the x direction having k-dependent hopping amplitudes, cf. Eq. (3).

Explicit usage of hopping matrix in Eq. (1) for the lattice Green's function leads to artifacts if it is truncated to a finite size matrix in order to proceed with the numerical calculations. To overcome this problem we add self-energy terms to the edge of the finite cluster to mimic the infinite environment in which this finite subsystem is embedded [7–9]. Due to the translation invariance along the DW direction it suffices to add the self-energy term $\Sigma_{\rm B-S}(z,k)$ which depends only on the frequency and the quasi-momentum k. Each k block describes a one-dimensional system with only nearest-neighbor k-dependent hopping and the formula for $\Sigma_{\rm B-S}(z,k)$ can be written in closed form:

$$\begin{aligned}\Sigma_{\rm B-S}(z,k) &= |t(e^{ik\frac{a}{2}} + e^{-ik\frac{a}{2}})|^2\, G_{\rm s-i}(z + 2t\cos(ka), k) = \\ &= \frac{z + 2t\cos(ka)}{2}\left(1 - \sqrt{1 - \frac{4|t(e^{ik\frac{a}{2}} + e^{-ik\frac{a}{2}})|^2}{(z + 2t\cos(ka))^2}}\right).\end{aligned} \qquad (4)$$

In Eq. (4) $G_{\rm s-i}$ denotes the surface Green's function of a semi-infinite chain[10].

Using the mixed basis and the boundary self-energy term, Eq. (1) becomes

$$\begin{aligned}\hat{\mathcal{G}}_{\rm latt}(z) = \frac{1}{2\pi}\int_{-\pi}^{\pi} dk \Big[&z - \hat{\Sigma}_{\rm DMFT}(z) - \\ &-\hat{\mathcal{H}}_{\rm kin}(k) - \hat{\Sigma}_{\rm B-S}(z - \Sigma^{x=\infty}_{\rm DMFT}(z), k)\Big]^{-1},\end{aligned} \qquad (5)$$

where $\hat{\Sigma}_{\rm DMFT}(z)$ is the self-energy matrix from the R-DMFT, $\hat{\mathcal{H}}_{\rm kin}(k)$ is the hopping matrix within a k block and $\hat{\Sigma}_{\rm B-S}(z - \Sigma^{x=\infty}_{\rm DMFT}(z), k)$ is the self-energy matrix describing the coupling to the bath. In the latter the energy is shifted by the self-energy term from the asymptotic limit ($x = \infty$) to include the correlations in the bulk. Here the assumption is made that at large distances from the domain wall its effects are damped out and the self-energy asymptotically approaches the homogeneous bulk results. Testing showed that this happens within 3-7 sites from the DW, thus the calculations in this work were done for systems where coupling $\Sigma_{\rm B-S}(z,k)$ to the bath was placed 20 lattice constants away from the DW.

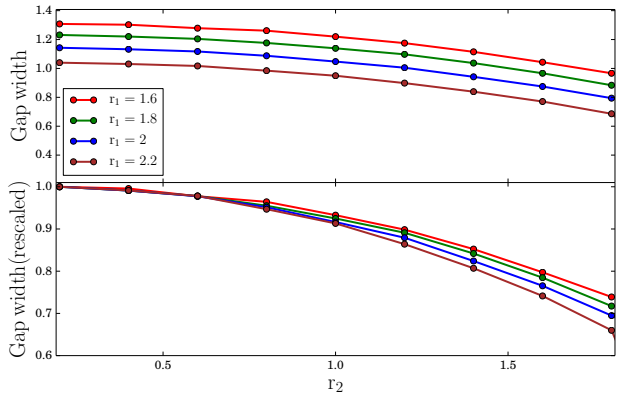

Figure 3. (Upper plot) Dependence of gap width on r_2 for different values of r_1. (Lower plot) Corresponding gap width rescaled by its maximal value.

The self-consistency equations for a set of effective impurity problems are solved using the numerical renormalization group [11, 12] with the discretization parameter $\Lambda = 2$. We work in units of the half-bandwidth $D = 9t/2$. Hubbard repulsion is $U = 4D$, while $U_{c,2} \approx 3D$ for the triangular lattice within the DMFT. The calculations are performed at zero temperature.

To account for the imperfections inside real DWs in 1T-TaS_2, in the calculations for the dimerized case we also include a constant purely complex term $\eta = -0.05i$ at the DW sites. The role of this additional term is to mimic the scattering caused by the presence of kinks or termination of the domain wall that differentiate it from the pristine infinite case used in modeling.

V. CHARGE GAP IN $r_1 \neq r_2$ CASE

In this section we discuss the influence of $r_1 \neq r_2$ on the Mott phase at the DW wall. Fig. 3 shows the evolution of the gap when one hopping ratio r_2 is varied and the other r_1 is kept fixed. Since the bare bandwidth (interval supporting both subbands) is given by $2(r_1 + r_2)$ and kinetic energy (in the first approximation) behaves as $\sqrt{r_1^2 + r_2^2}$, the shape of the curves in Fig. 3 clearly indicates that the later is indeed the energy scale controlling the gap width. To highlight this fact, we collapsed the curves for different r_1 onto each other by rescaling them by their largest value (lower panel in Fig. 3). For $r_2 < 1$ all curves display a very similar behaviour, but the deviation between them increases with increasing r_2.

VI. DETAILS ABOUT EXPERIMENTAL STM/STS MEASUREMENTS

The topographic images that show the David-star pattern are taken at a high bias voltage of $-800\,\mathrm{mV}$. We have investigated two examples of the domain walls: one (A) was found connecting two large-scaled defects and another (B) was found after the relaxation of the metallic mosaic phase. The David-star overlap in both DWs investigated is equal to one atomic lattice period.

The DW-A was characterized with the dI/dV map shown in the main text Fig. 1, as well as in Figs. 6(a),(c) and Fig. 5 in the Supplement. The map was obtained in the $\pm 0.6\,\mathrm{V}$ range with 0.5 nm spatial resolution using the lock-in technique with 25 mV AC modulation. The map, Fig. 5(c), allows to see that the substantial spatial variations of the spectral weight are present along the domain wall at all energies of interest around the Fermi level E_F.

The tunneling spectra for DW-B [Fig. 6(b),(d)] were taken with small DC bias steps and large integration time to obtain high resolution and avoid convolution with the AC lock-in modulation. The raw $I-V$ curves inside and outside the DW-B (L_0 and L_∞ in the main text) are shown in Fig. 4. Clear difference in slopes demonstrate the elevated Fermi-level LDOS. The sharp jump indicates the high value of the LDOS in the in-gap state compared to the background, by analogy with the occurrence of N-type $I-V$ curves in tunnel diodes.

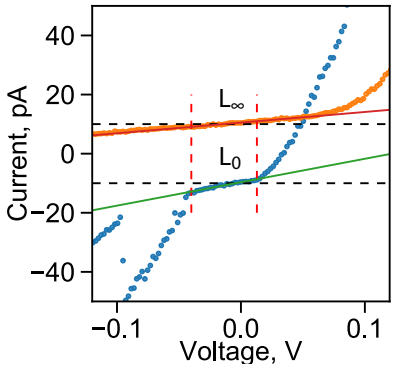

Figure 4. Comparison of the raw $I-V$ curves inside (blue, L_0) the DW-B and away from it (orange, L_∞). Solid lines are guide for eyes showing the slope around the Fermi level.

VII. COMPARISON OF THE DOMAIN WALLS OF DIFFERENT ORIGIN

Below we compare the two walls, DW-A and DW-B, in terms of the major spectral features discussed in the main text. The side-by-side comparison of the spectra is shown in Fig. 6.

- The band bending is observed for both DW-A and DW-B. Its direction is the same.
- Spectral reconstruction is found for both DW-A and DW-B.
- The sub-gap states in the occupied part of the spectrum are observed in both cases, although no sharp resonance can be resolved for DW-A. This is likely linked to the convolution with the AC modulation from lock-in.

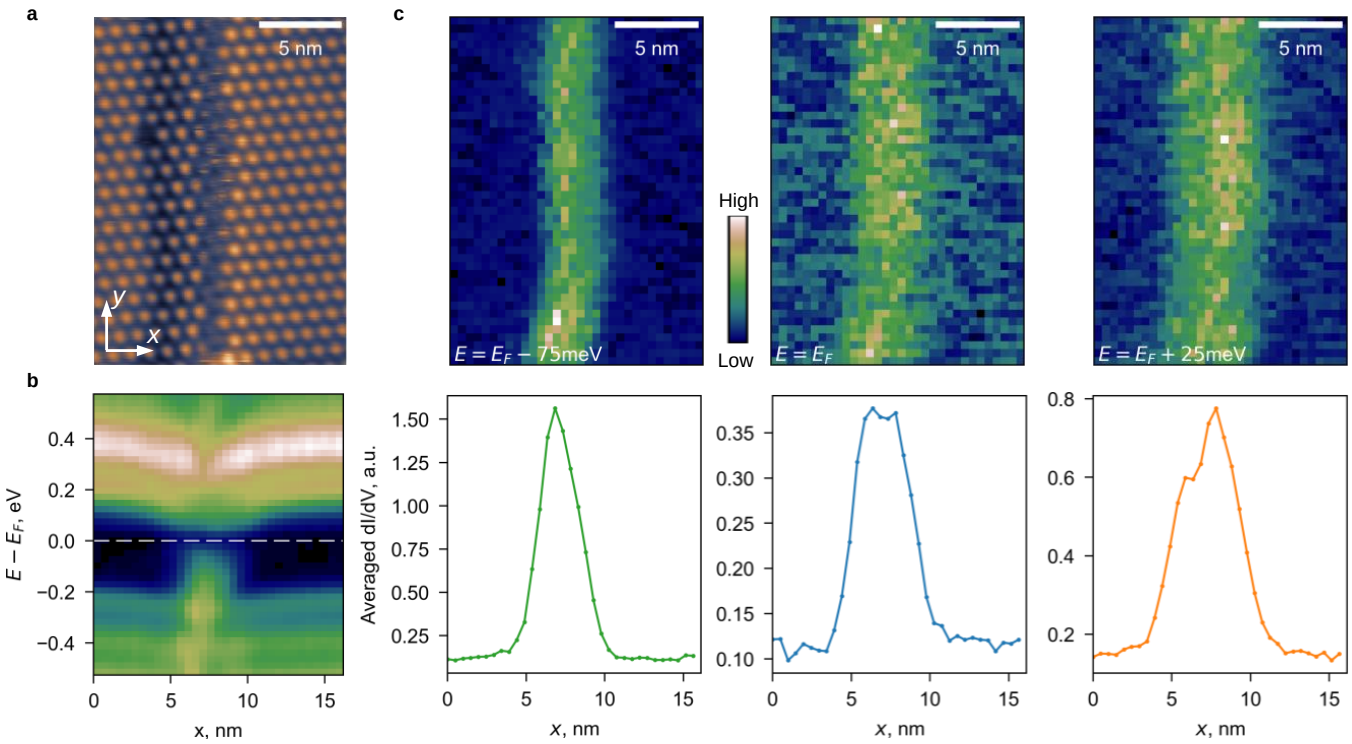

Figure 5. Spectroscopy maps for DW-A: a) Topographic image. b) Tunneling spectra evolution on crossing the wall from left to right in the x direction [see panel (a) for the coordinate axis orientation]. For each position x, the spectra are averaged along the wall direction y. c) Tunneling spectroscopy maps at selected energies within the split band emerging inside the domain wall. The plots in the second row show the evolution of the average LDOS at the respective energy on crossing the wall (for each x position the averaging is done along the wall direction y).

- Neither domain wall shows a significant change in the CDW E_V position.

In conclusion, the relevant physics is the same in both cases. The differences are: (i) the Fermi level position in the gap (which is sample dependent) and (ii) quantitative shape of the spectra (which is tip dependent).

In the DW-A case, the UHB comes very close to the Fermi level, see Fig. 7(a). It is interesting thus to compare the behavior with the predictions of the doping-driven metallization scenario. In the latter we would expect the appearance of a peak merged with the UHB lower edge. Experimentally, only minor increase of the spectral weight is observed above E_F, better seen if the spectra are subtracted, Fig. 7(b). It is almost indistinguishable from the UHB as is seen from comparing the spatial distribution with that at $E \leq E_F$. The behavior suggests that the hopping-driven scenario still dominates even in this case.

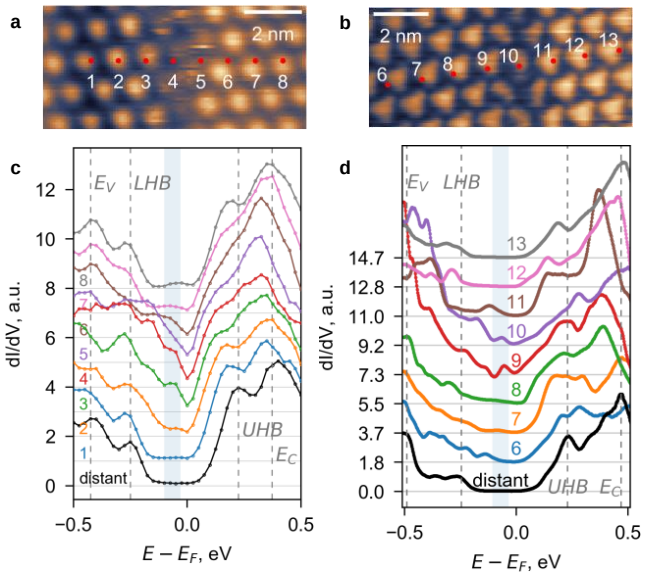

Figure 6. Comparison of the DW of different origin: a, b) Topographic images of the DW-A and DW-B, respectively. Red dots mark the positions where the spectra were taken. c, d) Individual spectra at different positions across the wall for DW-A and DW-B, respectively. The curves are offset for clarity. The black curve shows the spectrum observed far away from the domain wall. Dashed lines show the position of respective spectral features. The shaded area marks the energy of the in-gap state.

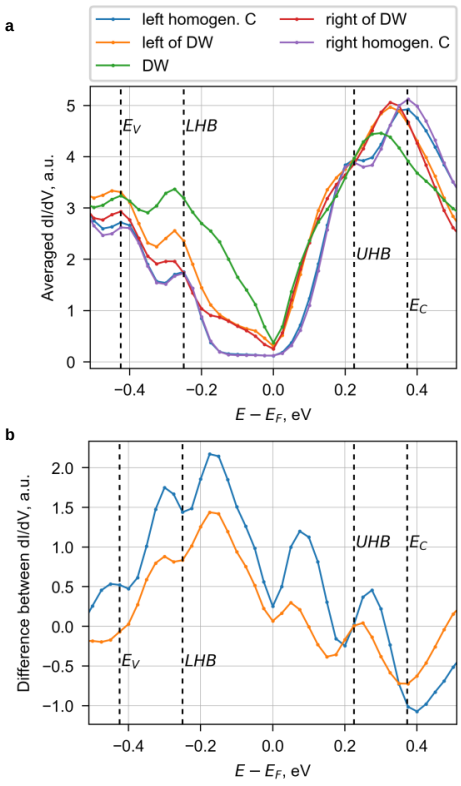

Figure 7. a) DW-A spectra spatially averaged in 5 different areas described in legend. b) Subtracted averaged spectra: blue – inside the DW and homogeneous C (green and blue curves in (a)); orange – inside the DW and left of DW (green and orange curves in (a)).

[1] Volker Heine, "$s-d$ interaction in transition metals," Phys. Rev. **153**, 673–682 (1967).

[2] K. Rossnagel and N. V. Smith, "Spin-orbit coupling in the band structure of reconstructed 1T-TaS_2," Phys. Rev. B **73**, 073106 (2006).

[3] L. Ma, C. Ye, Y. Yu, X. F. Lu, X. Niu, S. Kim, D. Feng, D. Tománek, Y.-W. Son, X. H. Chen, and Y. Zhang, "A metallic mosaic phase and the origin of Mott-insulating state in 1T-TaS_2," Nat. Comms. **7**, 10956 (2016).

[4] R. W. Helmes, T. A. Costi, and A. Rosch, "Kondo Proximity Effect: How Does a Metal Penetrate into a Mott Insulator?" Phys. Rev. Lett. **101**, 066802 (2008).

[5] P. Bakalov, D. Nasr Esfahani, L. Covaci, F. M. Peeters, J. Tempere, and J.-P. Locquet, "Electric-field-driven Mott metal-insulator transition in correlated thin films: An inhomogeneous dynamical mean-field theory approach," Phys. Rev. B **93**, 165112 (2016).

[6] Juho Lee and Chuck-Hou Yee, "Interfaces in coexisting metals and Mott insulators," Phys. Rev. B **95**, 205126 (2017).

[7] H. Ishida and A. Liebsch, "Embedding approach for dynamical mean-field theory of strongly correlated heterostructures," Phys. Rev. B **79**, 045130 (2009).

[8] H. Ishida and A. Liebsch, "Cluster dynamical mean-field study of strongly correlated heterostructures: Correlation-induced reduction of proximity effect," Phys. Rev. B **82**, 045107 (2010).

[9] M. Settnes, S. R. Power, J. Lin, D. H. Petersen, and A.-P. Jauho, "Patched green's function techniques for two-dimensional systems: Electronic behavior of bubbles and perforations in graphene," Phys. Rev. B **91**, 125408 (2014).

[10] M. M. Odashima, B. G. Prado, and E. Vernek, "Pedagogical introduction to equilibrium Green's functions: condensed-matter examples with numerical implementations," Rev. Bras. Ens. Fis. **39**, 1303 (2017).

[11] K. G. Wilson, "The renormalization group: Critical phenomena and the Kondo problem," Rev. Mod. Phys. **47**, 773 (1975).

[12] Ralf Bulla, Theo Costi, and Thomas Pruschke, "The numerical renormalization group method for quantum impurity systems," Rev. Mod. Phys. **80**, 395 (2008).